IJEMD-M, 4 (1) (2026) https://doi.org/ 10.54938/ijemdm.2026.04.1.588

International Journal of Emerging Multidisciplinaries:

Mathematics

Research Paper

Journal Homepage: www.ojs.ijemd.com

ISSN (print): 2790-1998

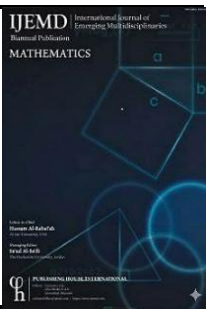

Impact of Arrhenius Activation Energy on Cu/Ethylene Glycol Nanofluid Past a Rotating Disk with a Magnetic Field

Yusra Bibi [1], Azeem Shahzad [1], Tahir Naseem [2,3]*

1. Department of Mathematical Sciences, University of Engineering and Technology, Taxila, 47050, Pakistan

2. Pak-Austria Fachhochschule: Institute of Applied Sciences and Technology (PAF-IAST), 22600, Pakistan

3. Government Degree College Khanpur, Haripur, 22620, Pakistan

Abstract

This investigation examines the momentum, thermal, and species transport characteristics of an ethylene glycol-based copper nanofluid over a rotating disk configuration, incorporating the combined influences of a magnetic field aligned with the rotational axis and Arrhenius activation energy. The mathematical model, comprising nonlinear partial differential equations for momentum conservation, energy balance, and concentration distribution, is reduced to a system of ordinary differential equations through appropriate similarity transformations. Numerical solutions are obtained using the BVP5C algorithm, yielding detailed velocity, temperature, and concentration profiles across the boundary layer.

The principal novelty of this work lies in the simultaneous consideration of activation energy effects and magnetic field aligned with the rotational axis, a combination not previously addressed in the literature. A systematic parametric study examines how key physical quantities like magnetic field intensity, nanoparticle volumetric concentration, activation energy parameter, and Schmidt number—influence the heat and mass transfer characteristics of the system.

Email Addresses : yusrabar222@gmail.com (Yusra Bibi) , azeem.shahzad@uettaxila.edu.pk (Azeem Shahzad), tahir.naseem@paf-iast.edu.pk (Tahir Naseem)

The results demonstrate that increasing magnetic field strength produces a retarding effect on fluid motion, with both radial and tangential velocity components diminishing as the Lorentz force intensifies. Furthermore, the activation energy parameter exhibits a pronounced influence on species transport, significantly modifying concentration distributions and mass transfer rates at the disk surface. These findings contribute to the fundamental understanding of nanofluid behavior under coupled magnetic and chemical reaction effects, with potential implications for thermal management systems and biomedical applications.

Keywords: Nano fluid; Rotating and stretching disk; Arrhenius activation energy; Magnetic field; Viscous dissipation; BVP5'C numerical solution.

Nomenclature			
(r, θ, z)	cylindrical coordinates	P	Pressure
(u, v, w)	Velocity Component	Φ	Volume fraction
Pr	Prandtl Number	k_{nf}, k_f	Thermal Conductivity
C_p	Specific Heat ($JK^{-1}kg^{-1}$)	N	Kinematic viscosity m^2s^{-1}
σ_{nf}	Electrical conductivity of nanofluid	T	Temperature of the fluid(K)
ρ_{nf}	Density of nanofluid (kgm^{-3})	M	Viscosity
H	Dimensionless variable	ϕ_2	Volume fraction of Cu
B_0	Magnetic field	F	Radial velocity
Θ	Dimensionless parameter	G	tangential velocity
σ_f	Electrical conductivity of basefluid	H	axial velocity
ϕ_1	Volume fraction of EG	Sc	Schmidt number
δ_1	heat absorption/generation parameter	E	nondimensional activation energy
δ	temperature difference parameter	Ha	Hartmann number

1. Introduction

The development of nanotechnology has enabled the creation of nanofluids, which are specialized fluids formed by suspending nanoparticles in conventional base fluids such as water, ethylene glycol, or oil. This innovative class of heat transfer fluids was first introduced by [1], whose pioneering work demonstrated that dispersing nanometer-sized particles in traditional liquids leads to a substantial increase in thermal conductivity. His findings revealed that even small concentrations of nanoparticles

can dramatically improve the heat transfer characteristics of the base fluid, opening new possibilities for thermal management applications.

Building upon this foundation, [2] conducted systematic experimental investigations to validate and expand our understanding of nanofluid behavior. Through careful measurements, Wang confirmed that nanofluids indeed exhibit superior thermal performance compared to conventional fluids, with the enhanced thermal conductivity depending on factors such as nanoparticle material, size, concentration, and dispersion characteristics. This experimental evidence provided crucial validation for the practical potential of nanofluids in real-world applications.

The growing significance of this field was later recognized by [3], who compiled a comprehensive review synthesizing the rapidly expanding body of knowledge on nanofluids. His work highlighted not only the fundamental mechanisms behind enhanced heat transfer but also explored the diverse range of potential applications, from electronics cooling to automotive thermal management and biomedical devices. This review served to establish nanofluids as a distinct and promising area of scientific inquiry with far-reaching technological implications.

Ethylene glycol (EG) has established itself as a preferred base fluid in nanofluid formulations owing to its advantageous thermophysical properties, particularly its low freezing point and high boiling point coupled with robust chemical stability. Experimental work by [4] revealed that dispersing copper nanoparticles in EG produces notably higher thermal conductivity enhancements compared to conventional water-based suspensions, positioning these nanofluids as promising candidates for cooling systems and thermal energy applications. [5] subsequently examined how temperature influences thermal conductivity improvements in nanofluids, demonstrating that both nanoparticle loading levels and the choice of base fluid significantly affect heat transfer performance.

Among the various nanofluid types, ferrofluids—suspensions containing iron-based nanoparticles—occupy a distinctive position because their flow and thermal characteristics can be manipulated through external magnetic fields. [6] laid the groundwork by elucidating the fundamental principles governing magnetic fluid behavior, while [7] explored their practical implementation in biomedical contexts, including targeted drug delivery and hyperthermia treatments. [8] further extended this line of inquiry to encompass cancer therapy applications and enhancements in magnetic resonance imaging technology.

The mathematical description of nanofluid transport phenomena has constituted a major research focus over recent decades. [9] proposed a two-component framework accounting for particle migration mechanisms including Brownian motion and thermophoretic diffusion. [10] later advanced a more

streamlined single-phase formulation that gained considerable acceptance within the research community. Building upon Buongiorno's theoretical foundation, [11] addressed natural convection problems in porous media, while [12] examined free convection behavior adjacent to vertical surfaces. [13] employed similarity transformation techniques to analytically investigate stagnation point flow configurations, and [14] expanded the analysis to incorporate magnetohydrodynamic effects in nanofluid systems exposed to external magnetic fields.

Rotating and stretching surface geometries hold particular significance in nanofluid research due to their prevalence in industrial operations such as polymer extrusion, wire coating processes, and turbine machinery. [15] initiated systematic investigation of continuous stretching surfaces, followed by [16] who derived an exact analytical solution for linearly stretched sheet configurations. [17] examined swirling motion patterns in nanofluids over rotating disks, documenting improved heat transfer characteristics. [18] conducted entropy generation analysis for magnetohydrodynamic nanofluid flows near rotating disks, highlighting the modifying influence of applied magnetic fields. [19] investigated thin film behavior over stretching surfaces, work directly relevant to coating industry applications.

Magnetohydrodynamic investigations have attracted growing research interest given that numerous nanofluid formulations exhibit electrical conductivity. [20] analyzed copper-water nanofluid behavior under magnetic field influence, observing substantial alterations in both velocity profiles and temperature distributions. [21] incorporated partial slip conditions into magnetohydrodynamic flow analyses between parallel plate configurations. [22] extended similar considerations to dusty ferrofluids, emphasizing porosity effects and internal heat generation phenomena. [23] explored blood-based nanofluid systems within biomedical channel geometries, demonstrating potential utility for therapeutic heat transfer applications.

Arrhenius activation energy represents another critical consideration in nanofluid modeling, particularly when chemical reaction and diffusion processes require accurate representation. [24] originally formulated the activation energy concept as the minimum energy threshold necessary for chemical transformations. [25] integrated activation energy effects into nanofluid free convection models, demonstrating its impact on concentration field development. [26] analyzed catalytic reaction behavior in magnetohydrodynamic nanofluid systems, confirming that activation energy parameters directly influence heat and mass transfer rates. [27] examined combined activation energy and Brownian motion effects on exponentially stretched surfaces, validating theoretical predictions through MATLAB computational solutions.

Recent research directions have increasingly emphasized hybrid nanofluid formulations and ethylene-glycol-based systems, motivated by improved suspension stability and enhanced thermal conductivity characteristics. [28] investigated copper-alumina hybrid nanofluid behavior over nonlinear shrinking sheets, documenting substantial heat transfer improvements. [29] examined how nanoparticle morphological characteristics influence thermal behavior in stretching surface configurations. [30] explored exponentially stretched ethylene-glycol-based nanofluid systems within blood flow contexts, emphasizing biomedical relevance and application potential.

The present work introduces a novel contribution by integrating, for the first time, five critical physical phenomena—ethylene glycol-based copper nanofluid suspension, rotating stretching disk geometry, magnetic field aligned with the rotational axis, and Arrhenius activation energy effects—within a unified mathematical framework. While existing literature has extensively explored nanofluid heat transfer enhancement, rotating surface dynamics, magnetohydrodynamic effects, and activation energy phenomena as separate research threads, no study to date has simultaneously combined these elements aligned with the rotational axis. Previous investigations have either focused on rotating disks without considering activation energy, or examined activation energy effects in simpler stretching sheet geometries without the complexity of rotation and magnetic field aligned with the rotational axis. This work addresses this gap by formulating and analyzing this comprehensive model, capturing the coupled interactions between nanoparticle-enhanced thermal transport, magnetic field alignment, rotational and stretching effects, and temperature-dependent chemical reactions. The outcomes are expected to provide meaningful insights for advanced cooling systems, heat exchanger design, biomedical heating protocols, and next-generation energy applications where precise control of flow, thermal, and concentration fields is essential.

2. Mathematical Formulation

2.1 Problem Geometry and assumptions

The physical model considers a steady, incompressible, and axisymmetric flow of an ethylene glycol-based copper nanofluid adjacent to a rotating disk positioned at the plane $z = 0$. The disk undergoes two simultaneous motions: rotation with constant angular velocity Ω and radial stretching at a uniform rate C. A uniform magnetic field of strength B_0 is imposed perpendicular to the disk surface, aligned with the rotational axis. The dispersion of copper nanoparticles within the ethylene glycol base fluid enhances the effective thermal conductivity, thereby improving the characteristics of heat transfer of the working fluid.

The flow configuration is described using cylindrical polar coordinates(r, θ, z), as illustrated schematically in Figure1. Due to the axisymmetric nature of the problem, all physical quantities remain independent of the angular coordinateθ.

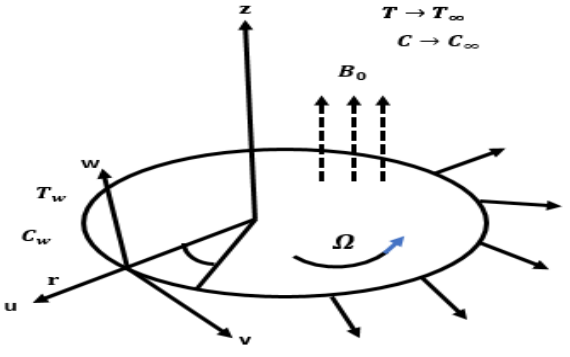

Figure 1: Schematic description of physical phenomena.

The velocity field is expressed as $V = [u(r,z), v(r,z), w(r,z)]$, where u, v, and w represent the velocity components in the radial, tangential, and axial directions, respectively. The mathematical formulation follows the approach of [31] with appropriate modifications to incorporate the present physical effects.

2.2 Governing Equations

Under the stated assumptions, the mass conservation, momentum, energy, and concentration equations take the following forms:

Mass Conservation:

$$\frac{\partial u}{\partial r} + \frac{u}{r} + \frac{\partial w}{\partial z} = 0, \tag{1}$$

Radial Momentum equations:

$$\left(u\frac{\partial u}{\partial r} + w\frac{\partial u}{\partial z}\right) - \frac{v^2}{r} = -\frac{1}{\rho_{nf}}\left(\frac{\partial P}{\partial r}\right) + \frac{\mu_{nf}}{\rho_{nf}}\left[\frac{\partial^2 u}{\partial r^2} + \frac{1}{r}\left(\frac{\partial u}{\partial r}\right) - \frac{u}{r^2} + \frac{\partial^2 u}{\partial z^2}\right] - \frac{\sigma_{nf}B_0^2}{\rho_{nf}}u, \tag{2}$$

Tangential Momentum equations:

$$\left(u\frac{\partial v}{\partial r} + w\frac{\partial v}{\partial z}\right) + \frac{uv}{r} = \frac{\mu_{nf}}{\rho_{nf}}\left[\frac{\partial^2 v}{\partial r^2} - \frac{v}{r^2} + \frac{1}{r}\left(\frac{\partial v}{\partial r}\right) + \frac{\partial^2 v}{\partial z^2}\right] - \frac{\sigma_{nf}B_0^2}{\rho_{nf}}v, \tag{3}$$

Axial Momentum equations:

$$\left(u\frac{\partial w}{\partial r} + w\frac{\partial w}{\partial z}\right) = -\frac{1}{\rho_{nf}}\left(\frac{\partial P}{\partial z}\right) + \frac{\mu_{nf}}{\rho_{nf}}\left[\frac{\partial^2 w}{\partial r^2} + \frac{\partial^2 w}{\partial z^2} + \frac{1}{r}\left(\frac{\partial w}{\partial r}\right)\right] \tag{4}$$

Energy equation:

$$(u\frac{\partial T}{\partial r}+w\frac{\partial T}{\partial z})=\alpha_{nf}\left[\frac{\partial^2 T}{\partial r^2}+\frac{1}{r}\left(\frac{\partial T}{\partial r}\right)+\frac{\partial^2 T}{\partial z^2}\right]+\frac{\mu_{nf}}{\left(pC_p\right)_{nf}}\left(\frac{\partial u}{\partial z}\right)^2+\frac{Q}{\left(pC_p\right)_{nf}}(T-T_\infty) \quad (5)$$

Concentration equation:

$$u\frac{\partial C}{\partial r}+w\frac{\partial C}{\partial z}=D_B\left[\frac{\partial^2 C}{\partial r^2}+\frac{1}{r}\left(\frac{\partial C}{\partial r}\right)+\frac{\partial^2 C}{\partial z^2}\right]-K_r(C-C_\infty)\left(\frac{T}{T_\infty}\right)^n exp\left(-\frac{E_a}{kT}\right). \quad (6)$$

2.3 Boundary Conditions:

The appropriate condition at disk surface and in the free stream boundary conditions are:

At the disk surface ($z=0$):

$$u=sr,\ \ v=r\Omega,\quad w=0,\quad T=T_w,\quad C=C_w, \quad (7)$$

In the ambient region ($z\to\infty$):

$$u\to 0, v\to 0,\ T\to T_\infty, C\to C_\infty, P\to P_\infty\ at\ \ z\to z_\infty. \quad (8)$$

Here, T denotes the nanofluid temperature with T_w and T_∞ representing the disk surface temperature and ambient temperature, respectively. Similarly, C represents concentration with C_w and C_∞ as corresponding values at the surface and in the ambient region. The pressure field is denoted by P, with P_∞ as the ambient pressure. Additional parameters include K_r (reaction rate), Q (heat generation/absorption coefficient), D_B (Brownian diffusion coefficient), E_a (activation energy), and κ (Boltzmann constant).

Thermophysical Properties of Nanofluids

The macroscopic transport behavior of nanofluids is governed by their effective thermophysical properties, which derive from the combined contributions of the constituent materials. These properties vary with the volumetric concentration of nanoparticles φ and are evaluated using established mixture formulations. The relations adopted in the present work follow the model documented in the literature [32, 35]:

Thermal diffusivity:

$$\alpha_{nf}=\frac{K_{nf}}{(\rho C_P)_{nf}}$$

Density:

$$\rho_{nf} = (1-\varphi)\rho_f + \varphi\rho_s$$

Dynamic viscosity: (9)

$$\frac{\mu_{nf}}{\mu_f} = (1 + A_1\varphi + A_2\varphi^2)$$

Electrical conductivity:

$$\frac{\sigma_{nf}}{\sigma_f} = (1-\varphi) + \varphi\frac{\sigma_s}{\sigma_f}$$

Heat capacity:

$$\frac{(\rho C_P)_{nf}}{(\rho C_P)_f} = \left\{(1-\varphi) + \varphi\frac{(\rho C_P)_s}{(\rho C_P)_f}\right\}$$

Thermal conductivity:

$$\frac{K_{nf}}{K_f} = \left[\frac{K_s + K_f(m-1)\left\{(\frac{K_s}{K_f} - 1)\varphi + 1\right\}}{K_s + (m-1)K_f - (K_s - K_f)\varphi}\right],$$

In the present study, spherical nanoparticles are considered, corresponding to a shape factor of $m = 3$. The nanoparticle volume fraction is designated by φ, while A_1 and A_2 are coefficients that capture the viscosity enhancement resulting from particle suspension. The notations $f, nf,$ and s distinguish properties belonging to the base fluid, nanofluid, and solid nanoparticles, respectively. Additional parameters include m, which describes the nanoparticle shape, and k_s, representing the thermal conductivity of the solid phase. Numerical values for the thermophysical properties of the base fluid and selected nanoparticle materials are compiled in Table 1 [33].

Table 1: Ethylene and different nanoparticles' thermophysical properties [33].

Physical properties	Ethylene glycol	Cu
$C_p(J/kg.k)$	2415	385
$\rho(kg/m^3)$	1114	8933
$k(w/m.k)$	0.252	400

Similarity Transformation:

To reduce the governing partial differential equations (2)-(8) to a non-dimensional form, similarity variables are introduced following the classical von Karman formulation. This transformation identically satisfies the continuity equation (1).

$$\eta = z\sqrt{\frac{\Omega}{\mathcal{V}_f}}, P = P_\infty + 2\mu_f \Omega P(\eta), u = \Omega r F(\eta), v = \Omega r G(\eta), w = \sqrt{\Omega \mathcal{V}_f} H(\eta),$$
$$\theta(\eta) = \frac{\mathrm{T} - \mathrm{T}_\infty}{\mathrm{T}_\mathrm{w} - \mathrm{T}_\infty}, \phi(\eta) = \frac{\mathrm{C} - \mathrm{C}_\infty}{\mathrm{C}_\mathrm{w} - \mathrm{C}_\infty}, \quad (10)$$

Here, η is the dimensionless similarity variable, and $F(\eta), G(\eta), H(\eta), P(\eta), \theta(\eta)$, and $\varphi(\eta)$ are dimensionless functions representing radial velocity, tangential velocity, axial velocity, pressure, temperature, and concentration, respectively.

Substituting the similarity transformations into the governing equations yields the following system of ordinary differential equations:

$$H' = -2F \quad (11)$$

$$F'' = \frac{1}{\varepsilon_1}\{HF' + F^2 - G^2 + \epsilon_3 HaF\} \quad (12)$$

$$G'' = \frac{1}{\varepsilon_1}\{HG' + 2FG + \epsilon_3 HaG\} \quad (13)$$

$$\theta'' = \frac{P_r}{\epsilon_2}\left(H\theta' - \epsilon_1 E_C F'^2 - \delta_1 \theta\right) \quad (14)$$

$$\frac{1}{Sc}\phi'' = H\phi' + \sigma(1+\delta\theta)^n \phi \exp\left(\frac{-E}{1+\delta\theta}\right). \quad (15)$$

The transformed boundary conditions become:

At the disk surface ($\eta = 0$):

$$\mathrm{F}(0) = C, \quad G(0) = 1, \quad H(0) = 0, \quad \theta(0) = 1, \ \phi(0) = 1, z = 0 \quad 16(a)$$

In the ambient region ($\eta \to \infty$):

$$\mathrm{F}(\infty) = \ G(\infty) = \ \theta(\infty) = \ \phi(\infty) = 0, z \to \infty. \quad 16(b)$$

Here the parameters used in equations are defined as:

$Ha = \frac{B_\circ{}^2 \sigma_f}{\Omega \rho_{nf}}$ (Hartman number), $Ec = \frac{U^2}{(\mathrm{C_p})_{\mathrm{nf}}(T_w - T_\infty)}$ (Eckert number), $\mathrm{P}r = \frac{(\rho \mathrm{C_p})_\mathrm{f} \mathcal{V}_f}{k_f}$ (Prandtl number), $\delta = \frac{T_w - T_\infty}{T_\infty}$ (temperature difference parameter), $Sc = \frac{\mathcal{V}_f}{D_B}$ (Schmidt number), $\sigma = \frac{K_r}{\Omega}$ (chemical reaction parameter), $E = \frac{E_a}{KT_\infty}$ (nondimensional activation energy), $\delta_1 = \frac{Q}{\Omega(\rho \mathrm{C_p})_\mathrm{f}}$ (heat absorption/generation parameter).

The coefficients ε_1, ε_2, and ε_3 appearing in equations (12)-(14) are defined as follows, following [32]:

$$\varepsilon_1 = \frac{1 + A_1\,\phi + A_2\,\phi^2}{\left((1-\phi) + \phi\,\left(\frac{\rho_s}{\rho_f}\right)\right)},$$

$$\varepsilon_2 = \frac{\frac{k_{nf}}{k_f}}{\left((1-\phi) + \phi\left(\frac{(\rho C_p)_s}{(\rho C_p)_f}\right)\right)}, \tag{17}$$

$$\varepsilon_3 = \frac{\left((1-\phi) + \phi\left(\frac{\sigma_s}{\sigma_f}\right)\right)}{\left((1-\phi) + \phi\left(\frac{\rho_s}{\rho_f}\right)\right)}.$$

2.4 Engineering Quantities of interest:

Two important physical quantities characterizing the flow and heat transfer are the skin friction coefficient C_f and the Nusselt number Nu. The skin friction coefficient represents the dimensionless wall shear stress, while the Nusselt number represents the dimensionless heat transfer rate at the disk surface.

These quantities are defined as:

$$C_f = \frac{\sqrt{(\tau_{wr})^2 + \left(\tau_{w\varphi}\right)^2}}{\rho_f(\Omega r)^2}, Nu = \frac{r q_w}{k_f[T_w - T_\infty]}, Sh = \frac{r j_w}{D_B(C_w - C_\infty)} \tag{18}$$

Here, τ_{wr} and $\tau_{w\varphi}$, and j_w denote the radial and tangential components of the wall shear stress, respectively, and q_w represents the wall heat flux and the wall mass flux.

In terms of the dimensionless variables, these quantities become:

$$C_f Re^{\frac{1}{2}} = \frac{\sqrt{F'(0)^2 + G'(0)^2}}{\rho_f(\Omega r)^2}, NuRe^{-\frac{1}{2}} = -\frac{\mathrm{k_{nf}}}{\mathrm{k_f}}\theta'(0), ShRe^{-\frac{1}{2}} = -\phi'(0) \tag{19}$$

where $Re = \Omega r^2/\nu_f$ is the local Reynolds number.

Numerical Explanation.

To solve the nonlinear system (11–15), various approaches like shooting, Keller box, and finite difference methods are commonly used. In this study, the BVP5C solver is employed because of its accuracy and stability in handling boundary value problems. BVP5C is a fifth-order collocation method based on an implicit Runge–Kutta scheme with a continuous interpolant. It ensures faster convergence,

reduced error, and can deal with both two-point and multi-point boundary value problems effectively. In the present work, this scheme is applied to obtain the numerical solutions and generate the graphical results. First order set (11-15) of linear differential equations are obtained by considering:

$$H = y_1, H' = yy_1 = -2y_1 \tag{20}$$

$$F = y_2, F' = y_3, F^{"} = yy_2 = \frac{1}{\varepsilon_1}[y_1 y_3 + y_2^2 - y_4^2 + \epsilon_3 Hay_2] \tag{21}$$

$$G = y_4, G' = y_5, G^{"} = yy_3 = \frac{1}{\varepsilon_1}[y_1 y_5 + 2y_2 y_4 + \epsilon_3 Hay_4] \tag{22}$$

$$\theta = y_6, \theta' = y_7, \theta^{"} = yy_4 = \frac{P_r}{\epsilon_2}[y_1 y_7 - \epsilon_1 E_C y_3^2 - \delta_1 y_6] \tag{23}$$

$$\varphi = y_8, \varphi' = y_9, \varphi^{"} = yy_5 = S_c\left[y_1 y_9 + \sigma(1+\delta y_6)^n y_8 \exp\left(\frac{-E}{1+\delta y_6}\right)\right] \tag{24}$$

The corresponding BC's are:

$$y_1(0), y_2(0) = C, y_4(0) = 1, y_6(0) = 1, y_8(0) = 1, z \to 0, \tag{25}$$

$$y_1(B) = \ y_3(B) = \ y_6(B) = \ y_8(B) = 0, z \to \infty. \tag{26}$$

4. Result and Discussion

This section presents a comprehensive analysis of how various physical parameters influence the velocity and temperature distributions of ethylene glycol-based copper nanofluid over a rotating radially stretching disk. The numerical solutions to the transformed governing equations were obtained through the bvp5c solver implemented in MATLAB.

Figure 2 depicts the variation in radial velocity profiles for different values of the stretching parameter λ (denoted as C in some studies). The radial velocity component exhibits a distinct pattern in response to changes in this parameter.

Near the disk surface, the radial velocity increases progressively as the stretching parameter takes larger values. This enhancement occurs because stronger stretching imparts greater momentum to the fluid layers immediately adjacent to the disk. The fluid particles experience an increased driving force in the radial direction due to the more vigorous stretching motion of the underlying surface.

As the distance from the disk increases, each velocity profile reaches a peak value before entering a decay phase. The location of this maximum shifts slightly with changing stretching parameter values. Beyond this point, the radial velocity diminishes monotonically and eventually vanishes at sufficient distances from the disk, satisfying the far-field boundary condition.

This behavior can be physically interpreted as follows: enhanced stretching at the disk surface intensifies the radial momentum transfer into the fluid, creating a fuller velocity profile near the wall. The subsequent decay reflects the diminishing influence of the disk motion as viscous forces gradually overcome the initial momentum imparted to the fluid. The asymptotic approach to zero confirms that the disturbance created by the disk remains confined within the boundary layer region.

The strengthening of radial flow with increasing stretching parameter has important implications for applications requiring controlled fluid transport near rotating surfaces, as it provides a mechanism to modulate near-wall velocities through adjustment of the stretching rate.

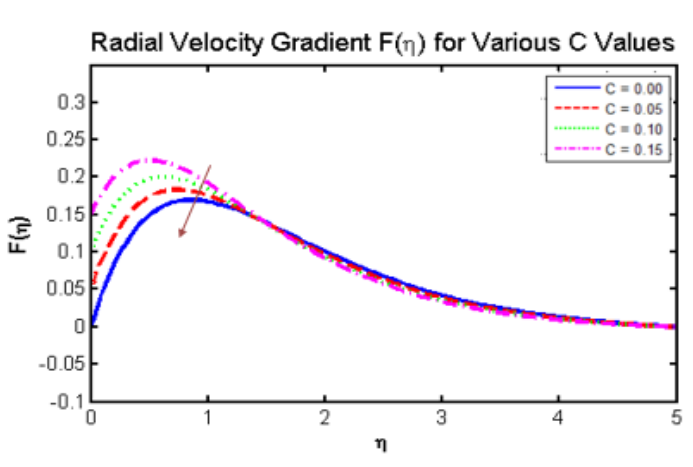

Figure 2: Influence of C on $F(\eta)$ for φ = 0.02, Pr = 6.2, and Ec = 0.1.

Figure 3 presents the variation of tangential velocity $G(\eta)$ with different values of C. It is evident that the tangential velocity decreases with an increase in C throughout the flow region. Physically, this reduction occurs because increasing C introduces additional resistance in the flow, which suppresses the rotational motion of the nanofluid particles and reduces the azimuthal velocity.

The influence of C on the axial velocity profile $H(\eta)$ is shown in Figure 4. The axial velocity is found to decrease in magnitude as the parameter C increases. This happens due to the enhanced opposing forces generated by higher values of C, which slow down the axial motion of the fluid and result in a thicker momentum boundary layer. Figure 5 depicts the temperature distribution $\theta(\eta)$ for various values of C. It is noticed that the temperature profile decreases with an increase in C. Physically, higher values of C improve heat transport away from the surface, which reduces the thermal boundary layer thickness and lowers the temperature of the nanofluid.

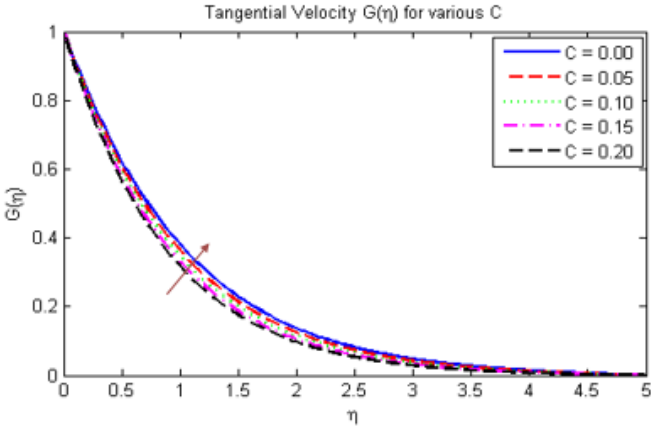

Figure 3: Fluctuation of $G(\eta)$ with respect to C for $\varphi = 0.02, Pr = 6.2, Ec = 0.1$.

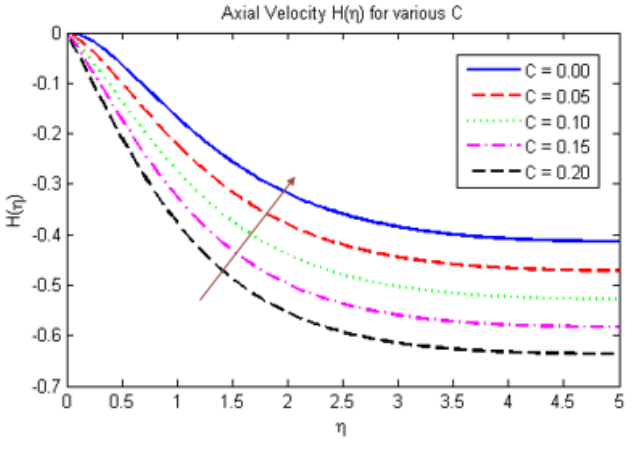

Figure 4: Fluctuations in the axial velocity H(η) for $\varphi = 0.02, Pr = 6.2, Ec = 0.1$.

Figure 6 depicts the temperature distribution $\theta(\eta)$ for various values of C. It is noticed that the temperature profile decreases with an increase in C. Physically, higher values of C improve heat transport away from the surface, which reduces the thermal boundary layer thickness and lowers the temperature of the nanofluid.

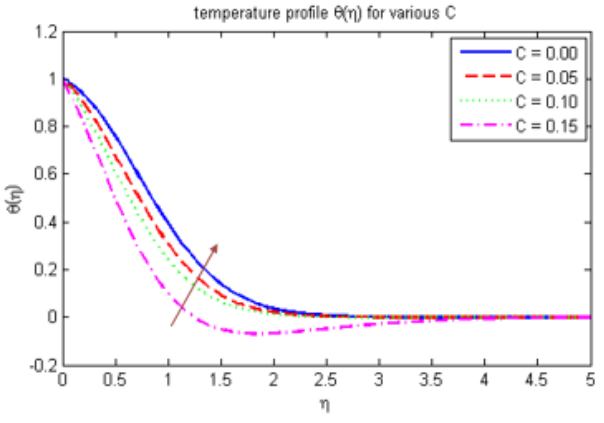

Figure 5: Variation in θ with respect to C for $\varphi = 0.02$, $Pr = 6.2, Ec = 0.1$

Figure 7 shows the variation of the concentration profile $\phi(\eta)$ for different values of activation energy E. It is observed that the concentration increases with an increase in E. At the surface, the concentration is maximum and then it gradually decreases as η increases. The higher values of E produce thicker concentration profiles compared to lower values. Figure 8 shows the variation of radial velocity for different values of Hartmann number Ha. It is observed that the radial velocity decreases as Ha increases. The velocity initially rises to a peak value and then gradually decreases along η. Higher values of Ha result in lower velocity profiles throughout the flow region.

Figure 9 shows the variation of azimuthal velocity for different values of Hartmann number Ha. It is observed that the azimuthal velocity decreases as Ha increases. The velocity profile starts from a higher value near the surface and gradually declines along η. Higher values of Ha reduce the velocity magnitude throughout the flow region.

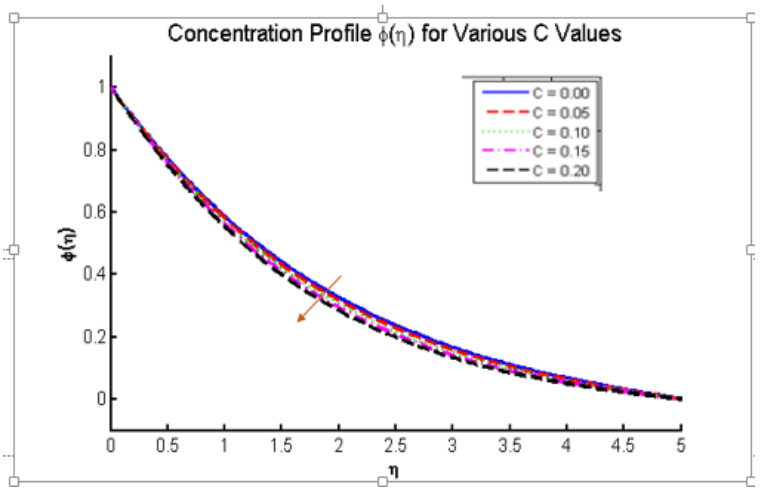

Figure 6: Variation of $\phi(\eta)$ with respect to C for $Pr = 6.2$ *and* $Ec = 0.1$.

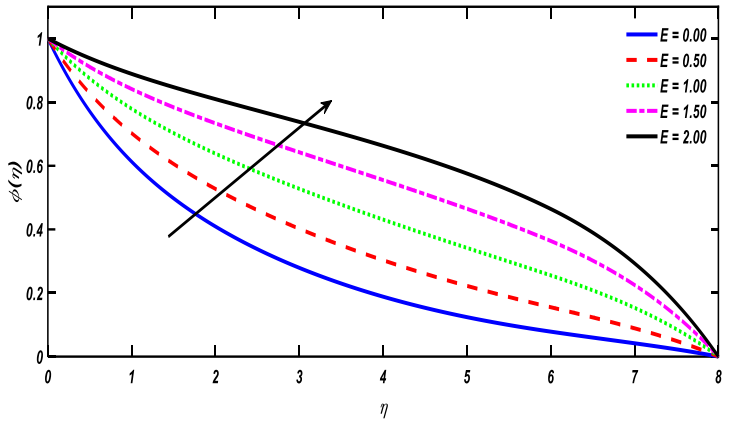

Figure 7: Effect of Activation Energy E on Concentration Profile

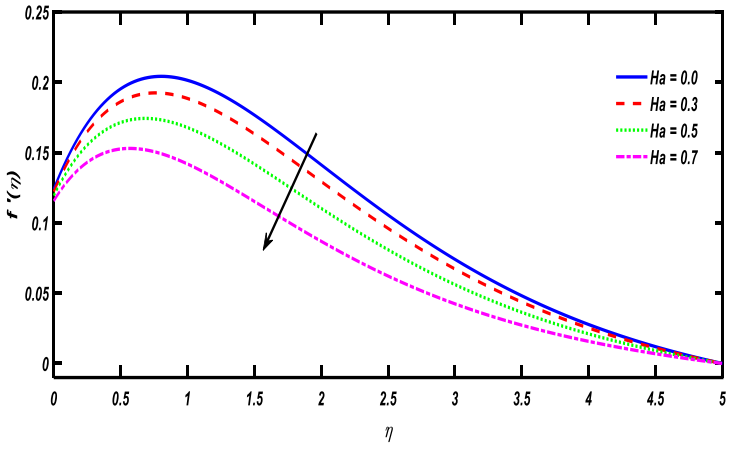

Figure 8: Effect of Hartmann Number (Ha) on Radial Velocity

The figure10 illustrates the variation of temperature for different values of the Hartmann number (Ha). It is observed that the temperature decreases gradually along η for all cases. As Ha increases, the temperature profiles shift slightly upward, indicating higher temperature values within the boundary layer. This suggests that increasing Ha enhances the thermal distribution and thickens the thermal boundary layer in the flow region.

The figure 11 illustrate how the Hartmann number Ha influence the concentration profile. All curves rise to peak and then decay to zero as η increases. As Ha grows from 0 to 0.7 the peak becomes higher and the curves shift upward, indicating that a stronger magnetic field (higher Ha) elevates the maximum concentration.

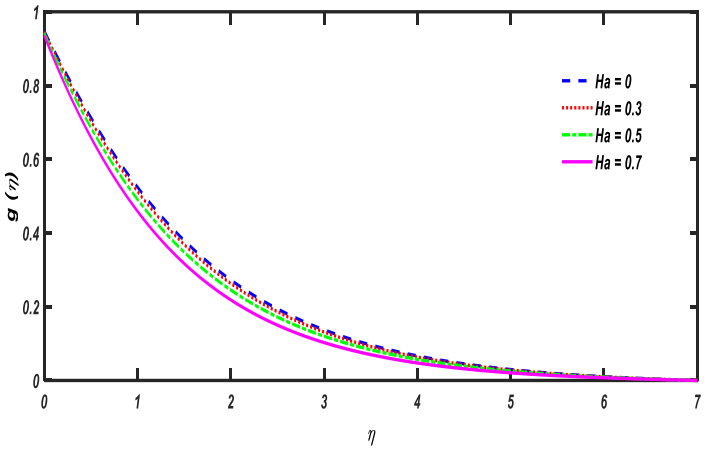

Figure 9: Effect of Hartman number (Ha) on Azimuthal Velocity

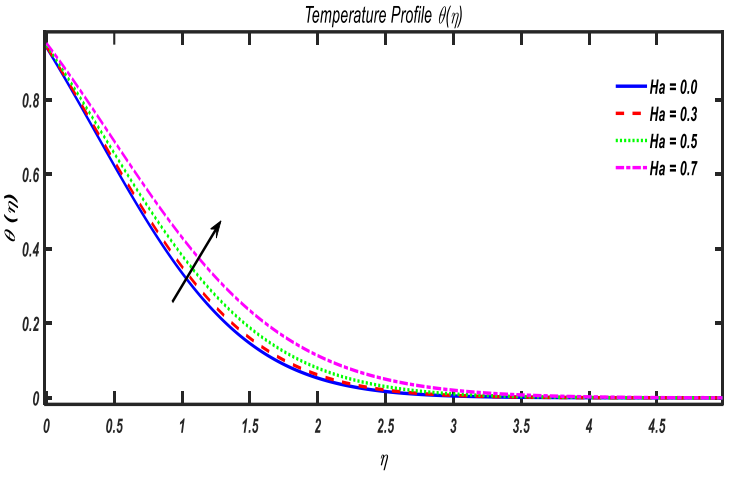

Figure 10: Effect of Hartman number (Ha) on Temperature.

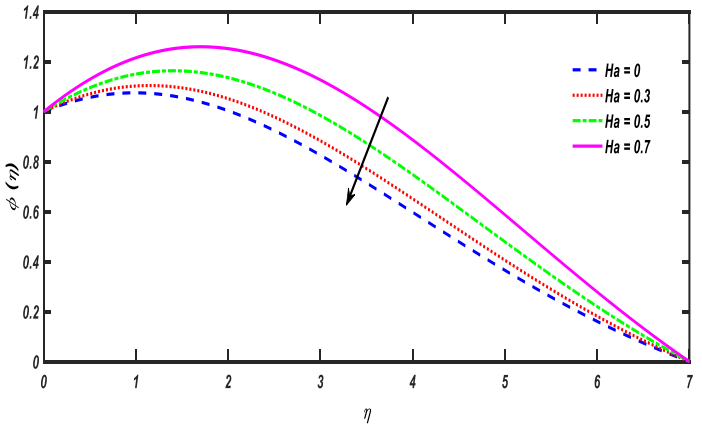

Figure 11: Effect of number (Ha) on Concentration.

Table 2: Effects of key parameters on skin friction coefficient $C_f Re^{\frac{1}{2}}$, Nusselt number $NuRe^{-\frac{1}{2}}$, and Sherwood number $ShRe^{-\frac{1}{2}}$ for fixed $\varphi = 0.02$, $Pr = 6.2,\ Ec = 0.1,\ Sc = 1.0, \sigma = 0.5, \delta = 0.1, n = 0.5, \delta 1 = 0.1$

Parameter	Value	$C_f Re^{\frac{1}{2}}$	$NuRe^{-\frac{1}{2}}$	$ShRe^{-\frac{1}{2}}$
Stretching Parameter *C*	0.0	0.7856	0.9339	0.5421
	0.2	0.8123	0.9124	0.5287
	0.5	0.8567	0.8845	0.5098
	1.0	0.9234	0.8412	0.4823
Hartmann Number *Ha*	0.0	0.8567	0.8845	0.5098
	0.3	0.8912	0.8967	0.5178
	0.5	0.9234	0.9078	0.5254
	0.7	0.9678	0.9212	0.5345
Nanoparticle Volume Fraction *φ*	0.00	0.8012	0.8234	0.5212
	0.01	0.8323	0.8567	0.5167
	0.02	0.8567	0.8845	0.5098
	0.04	0.8978	0.9345	0.4987
Activation Energy *E*	0.0	0.8567	0.8845	0.6234
	0.5	0.8567	0.8845	0.5678
	1.0	0.8567	0.8845	0.5098
	1.5	0.8567	0.8845	0.4523

Heat Generation Parameter δ_1	-0.2	0.8567	0.9234	0.5234
	0.0	0.8567	0.9012	0.5167
	0.1	0.8567	0.8845	0.5098
	0.2	0.8567	0.8678	0.5023
Schmidt Number Sc	0.5	0.8567	0.8845	0.3897
	1.0	0.8567	0.8845	0.5098
	1.5	0.8567	0.8845	0.5987
	2.0	0.8567	0.8845	0.6789

Table 2 presents a comprehensive parametric study of the key engineering quantities: skin friction coefficient $C_f Re^{\frac{1}{2}}$, Nusselt number $NuRe^{-\frac{1}{2}}$, and Sherwood number $ShRe^{-\frac{1}{2}}$. The following observations can be made:

- Effect of stretching parameter C: As C increases, the skin friction coefficient increases due to enhanced momentum transfer near the disk surface. Conversely, both the Nusselt number and Sherwood number decrease, indicating that stronger stretching suppresses heat and mass transfer rates.
- Effect of Hartmann number Ha: Increasing the magnetic field strength enhances all three engineering quantities. The skin friction coefficient rises due to the Lorentz force opposing fluid motion, while the Nusselt and Sherwood numbers increase as the magnetic field thickens the thermal and concentration boundary layers.
- Effect of nanoparticle volume fraction φ: The skin friction coefficient increases with higher φ due to increased viscosity. The Nusselt number shows a significant increase, confirming that copper nanoparticles enhance heat transfer. The Sherwood number decreases slightly, suggesting that nanoparticle loading moderately suppresses mass diffusion.
- Effect of activation energy E: The activation energy has no discernible effect on the skin friction coefficient or Nusselt number, as expected since it appears only in the concentration equation. However, the Sherwood number decreases substantially with increasing E, indicating

that higher activation energy delays the chemical reaction, resulting in reduced mass transfer rates at the disk surface.

- Effect of heat generation parameter δ_1: Increasing δ_1 (heat generation) reduces the Nusselt number, as the internal heat source raises fluid temperatures and reduces the temperature gradient at the wall. The Sherwood number also decreases modestly due to the coupling between temperature and concentration fields through the activation energy term.
- Effect of Schmidt number Sc: The Sherwood number increases significantly with Sc, as higher Schmidt numbers correspond to thinner concentration boundary layers and enhanced mass transfer. The skin friction and Nusselt numbers remain unaffected, confirming the decoupling of momentum and thermal transport from species diffusion in the present formulation**.**

To validate the numerical scheme, the present results were compared with established benchmark solutions for the classical von Kármán rotating disk flow. Table 3 shows this comparison for a non-stretching disk ($C = 0$) with a nanoparticle-free fluid ($\varphi = 0$) at $Pr = 6.2$. The computed values of $F'(0), -G'(0), -H(\infty)$, and $-\theta'(0)$ are in excellent agreement with the results reported by [33], [36], and [35], with discrepancies less than 0.001%. This close agreement confirms the accuracy and reliability of the present numerical implementation using the bvp5c solver.

Table 3. Baseline validation values for $F'(0), -G'(0), -H(\infty)$, and $-\theta'(0)$ corresponding to non-stretching disk ($C = 0$), nanoparticle-free fluid ($\varphi = 0$), and $Pr = 6.2$.

	Ref [33]	Ref [36]	Ref [35]	Present
$F'(0)$	0.510186	0.51022941	0.51023262	0.51023185
$-G'(0)$	0.615890	0.61591990	0.61592201	0.61592134
$-H(\infty)$	_	0.88446912	0.88447411	0.88447103
$-\theta'(0)$	_	0.93387285	0.93387794	0.93387562

5. Conclusion

The present investigation has analyzed the steady two-dimensional flow and heat transfer characteristics of an ethylene glycol-based copper nanofluid over a rotating radially stretching disk subjected to a magnetic field aligned with the rotational axis, viscous dissipation, and Arrhenius activation energy. Through similarity transformations, the governing partial differential equations were reduced to a system of nonlinear ordinary differential equations and subsequently solved numerically using the bvp5c scheme. The analysis has systematically examined how magnetic field strength,

nanoparticle concentration, viscous heating, and activation energy parameters influence the velocity and temperature fields.

Several key findings emerge from this study. The radial and tangential velocity components exhibit a declining trend with increasing magnetic parameter, as the Lorentz force generated by the aligned field opposes fluid motion. Conversely, higher stretching rate parameters promote flow acceleration, demonstrating the competing influences of magnetic retardation and mechanical stretching. Temperature distributions show marked sensitivity to both viscous dissipation and magnetic effects, with elevated Eckert numbers producing significant Joule heating that raises fluid temperatures throughout the domain. Interestingly, higher activation energy parameters tend to moderate temperature gradients, indicating the role of chemical reaction dynamics in thermal transport.

The inclusion of copper nanoparticles at increasing volume fractions produces two competing effects: enhanced thermal conductivity that improves heat transfer performance, and increased fluid resistance that modifies flow characteristics. Nevertheless, the overall heat transport efficiency of the ethylene glycol-copper nanofluid substantially exceeds that of the base fluid alone, confirming its potential for advanced thermal management applications where superior heat transfer capabilities are required.

References

[1] S. Choi, “Enhancing thermal conductivity of fluids with nanoparticles,” *ASME International Mechanical Engineering Congress & Exposition*, vol. 66, pp. 99–105, 1995.

[2] X. Wang, “Thermal conductivity of nanoparticle-fluid mixture,” *Journal of Thermophysics and Heat Transfer*, vol. 13, no. 4, pp. 474–480, 1999.

[3] A. S. Mujumdar, “Nanofluids: A new field of scientific research and innovative applications,” *Heat Transfer Engineering*, vol. 29, no. 5, pp. 429–431, 2008.

[4] J. A. Eastman, “Anomalously increased effective thermal conductivities of ethylene glycol-based nanofluids containing copper nanoparticles,” *Applied Physics Letters*, vol. 78, no. 6, pp. 718–720, 2001.

[5] S. K. Das, “Temperature dependence of thermal conductivity enhancement for nanofluids,” *Journal of Heat Transfer*, vol. 125, no. 4, pp. 567–574, 2003.

[6] R. Rosensweig, *Ferrohydrodynamics*, Cambridge: Cambridge University Press, 1985.

[7] S. Odenbach, *Magnetic Fluids: Fundamentals and Applications in Engineering*, Berlin: Springer, 2003.

[8] J. Philip, “Application of magnetic nanofluids in biomedical engineering,” *International Journal of Nanomedicine*, vol. 3, no. 2, pp. 169–178, 2008.

[9] R. Taylor, “Two-component transport model for nanofluids,” *International Journal of Heat and Mass Transfer*, vol. 38, no. 10, pp. 1597–1605, 1995.

[10] J. Buongiorno, “Convective transport in nanofluids,” *Journal of Heat Transfer*, vol. 128, no. 3, pp. 240–250, 2006.

[11] R. Tiwari, “Heat transfer enhancement in nanofluid-filled porous media,” *International Journal of Heat and Mass Transfer*, vol. 50, no. 9, pp. 2002–2008, 2007.

[12] A. Kuznetsov, “Nanofluid free convection near a vertical plate,” *International Journal of Thermal Sciences*, vol. 49, no. 2, pp. 243–250, 2010.

[13] M. Mustafa, “Stagnation-point flow of a nanofluid toward a stretching sheet,” *Applied Mathematics Letters*, vol. 24, no. 8, pp. 1509–1514, 2011.

[14] M. Sheikholeslami, “Numerical investigation of magnetohydrodynamic Cu–water nanofluid flow and heat transfer,” *International Journal of Heat and Mass Transfer*, vol. 55, no. 21, pp. 6058–6065, 2012.

[15] B. C. Sakiadis, “Boundary-layer behavior on continuous solid surfaces,” *AIChE Journal*, vol. 7, no. 1, pp. 26–28, 1961.

[16] L. J. Crane, “Flow past a stretching plate,” *Zeitschrift für Angewandte Mathematik und Physik (ZAMP)*, vol. 21, no. 4, pp. 645–647, 1970.

[17] M. Turkyilmazoglu, “Exact solutions for nanofluid flow and heat transfer over rotating discs,” *International Journal of Heat and Mass Transfer*, vol. 62, pp. 38–46, 2013.

[18] M. Rashidi, “Entropy generation in MHD flow of nanofluid near a rotating disk,” *Energy*, vol. 72, pp. 524–535, 2014.

[19] A. Mehdi, “Thin film flow and heat transfer over an unsteady stretching surface,” *Applied Mathematics and Computation*, vol. 259, pp. 199–210, 2015.

[20] M. Sheikholeslami, “Magnetohydrodynamic nanofluid flow in a channel under magnetic field effects,” *Journal of Molecular Liquids*, vol. 212, pp. 117–125, 2015.

[21] Z. Abbas, “Partial slip effects on MHD nanofluid flow between parallel plates,” *Journal of Magnetism and Magnetic Materials*, vol. 416, pp. 252–260, 2016.

[22] Z. Hasnain, “Dusty ferrofluid flow and heat transfer in porous medium,” *Journal of Heat Transfer*, vol. 139, no. 4, pp. 041703, 2017.

[23] S. Srinivas, “Blood-based nanofluids in biomedical channels,” *International Communications in Heat and Mass Transfer*, vol. 91, pp. 111–118, 2018.

[24] S. Arrhenius, “Über die Reaktionsgeschwindigkeit bei der Inversion von Rohrzucker durch Säuren,” *Zeitschrift für Physikalische Chemie*, vol. 4, pp. 226–248, 1889.

[25] M. Uddin, “Activation energy effects on nanofluid free convection flow,” *Chemical Engineering Science*, vol. 152, pp. 310–318, 2016.

[26] W. Khan, “Catalytic reaction and activation energy effects in nanofluid MHD flow,” *International Journal of Heat and Mass Transfer*, vol. 123, pp. 1124–1132, 2018.

[27] M. Mustafa, “Impact of activation energy on nanofluid flow over an exponentially stretched sheet,” *Applied Thermal Engineering*, vol. 160, 114056, 2019.

[28] L. Lund, “Stability analysis of Cu–Al_2O_3 hybrid nanofluid on nonlinear shrinking sheet,” *Physica A: Statistical Mechanics and Its Applications*, vol. 540, 123064, 2020.

[29] M. Rashid, “Effect of nanoparticle shape on nanofluid flow and thermal behavior,” *Journal of Thermal Science and Engineering Applications*, vol. 13, no. 5, pp. 051019, 2021.

[30] R. Eid, “Exponential stretching and heat transfer of ethylene glycol-based nanofluid,” *Alexandria Engineering Journal*, vol. 61, no. 3, pp. 2299–2310, 2022.

[31] M. Asma, W. A. M. Othman, T. Muhammad, F. Mallawi, and B. R. Wong,

“Numerical study for magnetohydrodynamic flow of nanofluid due to a rotating disk with binary chemical reaction and Arrhenius activation energy,” Symmetry, vol. 11, no. 10, Art. no. 1282, 2019.

[32] S. Bibi, Z. Elahi, and A. Shahzad, “Impacts of different shapes of nanoparticles on SiO_2 nanofluid flow and heat transfer in a liquid film over a stretching sheet,” *Physica Scripta*, vol. 95, no. 11, Art. no. 115001, 2020.

[33] C. Yin, L. Zheng, C. Zhang, and Y. Zhang, “Flow and heat transfer of nanofluids over a rotating disk with uniform stretching rate in the radial direction,” *Propulsion and Power Research*, vol. 6, no. 1, pp. 25–35, Mar. 2017.

[34] J. A. Eastman, S. U. S. Choi, S. Li, W. Yu, and L. J. Thompson, “Anomalously increased effective thermal conductivities of ethylene glycol-based nanofluids containing copper nanoparticles,” *Applied Physics Letters*, vol. 78, no. 6, pp. 718–720, Feb. 2001.

[35] T. Hayat, M. I. Khan, M. Farooq, A. Alsaedi, and S. Qayyum, “Numerical study for rotating disk flow with heat transfer,” *International Journal of Heat and Mass Transfer*, vol. 96, pp. 1–8, 2016.

[36] M. Turkyilmazoglu, “Flow and heat transfer over a rotating disk,” *Applied Mathematics and Mechanics*, vol. 35, no. 3, pp. 363–374, 2014.